Integration of Distributed Energy Resources to Unbalanced Grids Under Voltage Sags With Grid Code Compliance

Alejandro Rolán, Santiago Bogarra, and Mostafa Bakkar

***Abstract*—The aim of this paper is to analyze the situations in which distributed power generation systems (DPGSs) based on renewable energy sources (RESs) can be controlled when operating under voltage sags. Analytical models for both solar photovoltaic (PV) system and doubly-fed induction generator (DFIG)-based wind turbine (WT) written in the complex form of the *Park* variables are given. Three kinds of control for the grid-side converter (GSC) of a PV system are compared: constant *forward* voltage control (CFVC), balanced *positive*-sequence control (BPSC) and the proposed BPSC with grid code requirements (BPSC-GCR). Regarding the rotor-side converter (RSC) of a DFIG-based WT, its controllability is studied considering three different-sized DFIG-based WT units: 6 MW (offshore), 2 MW (onshore) and 7.5 kW (setup). The converter limits are also considered. Simulations carried out in MATLAB reveal that a RES-based DPGS can achieve fault ride-through (FRT) when subject to a certain fault (i.e., with a specific duration and depth), but it may be uncontrollable for different-sized units operating under different faults without considering the grid code requirements. Finally, experimental results prove the robustness of the BPSC-GCR method to let GSCs of PV systems achieve FRT under sags.**

***Index Terms*—Distributed power generation systems, doubly-fed induction generator, fault ride-through, grid code, grid integration, PV energy, sags, unbalanced faults, wind energy.**

I. INTRODUCTION

GLOBAL warming caused by the burning of fossil fuels and the social awareness to overcome this problem has accelerated the path towards decarbonization in recent years. Renewable energy sources (RESs) generated 29% of global electricity in 2020 [1]. Studies reveal that this share is expected to be 33% by 2025 [2] and surpass 60% of total final energy consumption by 2050 [3]. In order to achieve that goal, distributed power generation systems (DPGSs) based on RESs, such as solar photovoltaic (PV) panels or wind turbines (WTs) based on doubly-fed induction generators (DFIGs), whose typical configuration [4] is shown in Fig. 1, have emerged as the eco-friendly solution versus traditional power systems with fuel-based large power plants.

Tripping was used in the past to prevent power converters of RES-based DPGSs from being damaged when operating under voltage sags; however, due to the increase in the grid penetration of RES units for the last years, disconnection from the grid is no longer possible, since blackouts would affect the power quality [5]. Then, in order to achieve fault ride-through (FRT) capability for WTs and PV systems, a proper control of three-phase inverters is needed for their grid integration [6].

Transmission system operators (TSOs) from several countries have redesigned their grid codes requirements. Take the examples of the grid codes elaborated by: the National Grid Electricity System Operator (Great Britain) [7]; Energinet (Denmark) for wind power plants [8] and PV power plants [9]; TenneT (the Netherlands and Germany) [10]; and Red Eléctrica (Spain) [11]. This paper considers the Spanish grid code [11] (see Fig. 2, where $\Delta V = \pm 10\%$ for transmission grids [12]). A comparison between the technical requirements for wind power integration of several countries around the world can be found in [13] and a similar study is developed in [14] for wind power integration in Europe, North America and Asia. A review of procedures for the verification of grid code compliance for the integration of renewable generation in grids from Australia, Denmark, Great Britain, Ireland and Spain is carried out in [15]. Further to this, studies have proposed control techniques for RES-based DPGSs to achieve FRT according to grid codes.

Regarding WT systems, [16] proposes a control technique for HVDC offshore WTs to meet grid code requirements by frequency modulation; [17] states the importance of wind forecasting to match power generation and demand within the frequency range imposed by grid codes; and [18] proposes a new wind farm topology based on the combination of a fixed-speed WT and a variable-speed WT, according to the USA grid code. Regarding PV systems, [19] compares different control strategies for PV systems operating under sags with emphasis on grid code requirements; [20] proposes a methodology to control PV systems under voltage sags, according to the Spanish grid code; and [21] proposes a control strategy for

Manuscript received January 7, 2021; revised May 21, 2021, August 7, 2021, and August 16, 2021; accepted August 21, 2021. This work was supported in part by the Spanish Ministry of Science, Innovation and Universities under Grant RTI2018-095720-B-C33, and in part by the Spanish Ministry of Economy and EU FEDER Funds under Grant DPI2017-84503-R. Paper no. TSG-00040-2021. *(Corresponding author: Alejandro Rolán.)*

Alejandro Rolán is with the Department of Automatic Control, Barcelona East School of Engineering, Technical University of Catalonia, 08019 Barcelona, Spain (e-mail: alejandro.rolan@upc.edu).

Santiago Bogarra and Mostafa Bakkar are with the Department of Electrical Engineering, School of Industrial, Aerospace and Audiovisual Engineering of Terrassa, Technical University of Catalonia, 08222 Terrassa, Spain (e-mail: bogarra@ee.upc.edu; mostafa.bakkar@upc.edu).

Color versions of one or more figures in this article are available at https://doi.org/10.1109/TSG.2021.3107984.

Digital Object Identifier 10.1109/TSG.2021.3107984

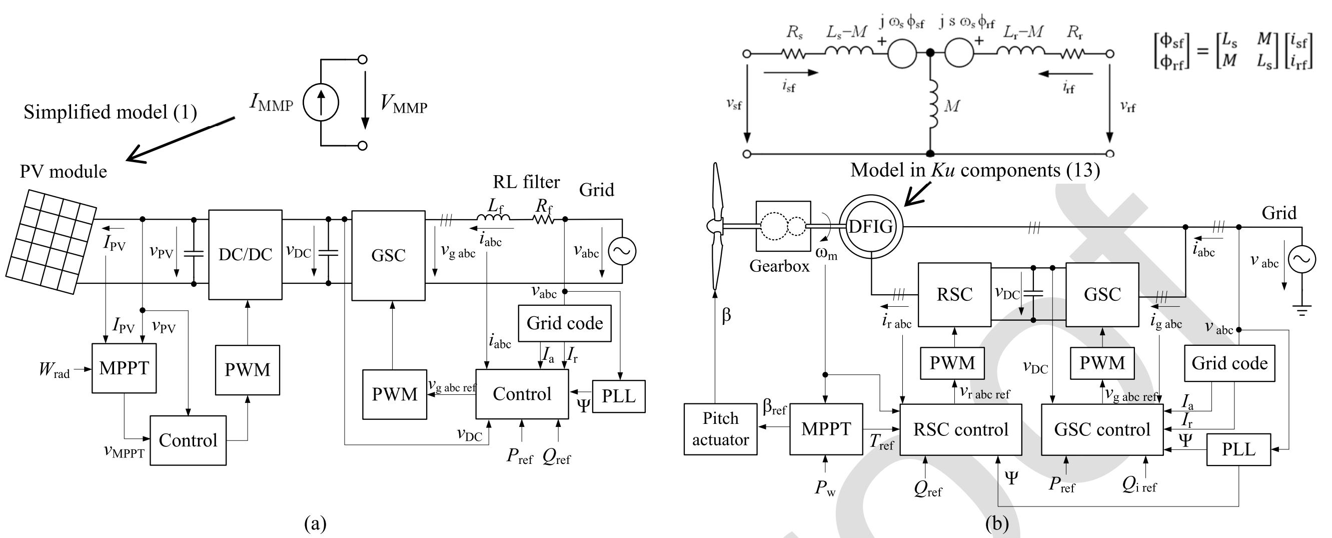

Fig. 1. Electrical scheme of the studied grid-connected RES-based DPGSs and their control, considering the grid code requirements. (a) PV system, and (b) DFIG-based WT. Passive sign convention. Acronyms: GSC = grid-side converter; MPPT = maximum power point tracking; PLL = phase-locked loop; PWM = pulse-width modulation; RSC = Rotor-side converter.

PV systems under voltage sags, according to the German grid code.

Some studies have also considered the voltage limit of the power converter to achieve FRT: [22] indicates critical values of sag parameters from which the controllability of DFIGs is lost, according to the voltage limit of the rotor-side converter (RSC); [23] considers the voltage limit of the RSC to explain analytically the behavior of DFIG-based WTs under unsymmetrical sags; [24] develops a similar study, but under symmetrical sags; [25] proposes a reference generator for distributed generation inverters under unbalanced faults; [26] proposes a control algorithm to limit initial overcurrent of DFIGs under sags without damaging the RSC; [27] analyzes the behavior of DFIGs under unbalanced conditions considering the voltage ratings of the RSC; and [28] analyzes the FRT of DFIGs under symmetrical sags and considers the RSC voltage to control the rotor current within its limit. Finally, only a few papers have paid attention to the effect of sag parameters (duration and depth) on the behavior of grid-connected RES-based DPGSs under grid faults: [19] analyzes the influence of sag parameters on the injected current of a three-phase inverter with grid code limitation; [22] indicates the values of sag parameters that cause the most severe effects on DFIG-based WTs; [23] analyzes the behavior of DFIGs under unsymmetrical sags and indicates the values of sag parameters under which the controllability is lost; [24] develops a similar study to [23], but with DFIG subject to symmetrical sags; [29] studies the voltage recovery process on three-phase inverters under sags with different parameters; [30] shows that different sag types with the same parameters cause different effects on the injected current by three-phase inverters; and [31] analyzes the effects of sag parameters on DFIG-based WTs under sags.

This paper uses the results of the authors' previous works regarding three-phase grid-connected inverters with grid code limitations [19]–[20], DFIG-based WTs under sags [22]–[24] and controllability of inverters under sags [29]–[30], but it goes a step further for two main reasons: (1) this paper proposes the use of a control strategy for three-phase inverters with the Spanish grid code (as in [19]), but it is suggests using the balanced *positive*-sequence control combined with the grid code requirements (named BPSC-GCR); (2) this paper studies the FRT of DFIG-based WTs with respect to its RSC, but unlike the authors' previous works [22]–[24], where the analysis was done for a 2-MW unit, in this paper three units are compared: 6 MW (offshore), 2 MW (onshore) and 7.5 kW (setup).

The contributions of this paper are: (1) to provide an analytical model for PV systems and DFIG-based WTs that describes their behavior under balanced and unbalanced grid conditions (Sections III–IV); (2) to propose a control strategy named BPSC-GCR) for the grid-side converter (GSC) of a PV system based on combining the balanced *positive*-sequence control with the grid code requirements (Section III); (3) to consider the converter voltage and current limits to obtain the sag durations and depths from which the controllability is lost (Section V); (4) to analyze the controllability according to different-sized DFIG-based WTs (Section V); and (5) to prove the robustness of the proposed control of GSCs for PV systems through experimental results (Section VI).

II. VOLTAGE SAGS

According to the IEEE Std. 1159-2019 [32], a sag (also known as dip) is defined as "a decrease in rms voltage to between 0.1 pu and 0.9 pu for durations from 0.5 cycles to 1 min". Originated mainly by faults, sags may cause saturation in transformers [33], large torque peaks in induction machines [34] and DC fluctuations and AC current peaks in voltage-source-inverter (VSI)-fed adjustable-speed drives (ASDs) [35].

A sag is characterized by four parameters [36]: depth (h), which is the remaining voltage with respect to the pre-fault voltage; duration (Δt), which is the time lapse from the beginning of a fault to its complete clearance, whose voltage recovery can be done abruptly or in different steps [37] (the former is assumed in this paper); fault current angle (ψ), which corresponds to the first instant of time in which current reaches zero (it varies from 75 deg to 85 deg in transmission grids [37], so a value of 80 deg is assumed in this paper); and typology, which is defined according to the type of fault that causes the sag: balanced faults (i.e., 3-phase faults or 3-phase-to-ground faults) cause balanced sags (type A), while unbalanced faults (i.e., 1-phase-to-ground faults, 2-phase faults or 2-phase-to-ground faults) cause unbalanced sags (types B…G) (Table I).

III. Grid-Connected PV System

A. Analytical Model of a Grid-Connected PV System

Fig. 1(a) shows the configuration of the PV system studied in this paper: a PV module connected to the grid through a front-end DC-DC boost converter and a grid-connected inverter (DC/AC or grid-side converter (GSC)) with an output RL filter.

The DC-DC boost converter is assumed to be ideally controlled by a maximum power point tracking (MPPT) algorithm [38], which is able to make the PV module operates at the knee of its I-V curve for standard conditions: solar irradiation W_{rad} =1 kW/m^2 at 25°C with AM (air mass) 1.5 solar spectrum [39]. Under these circumstances, the PV module plus the DC-DC boost converter can be modelled as a constant current source [40], whose current (I_{PV}) and voltage (V_{PV}) are

$$I_{\mathrm{PV}} = -I_{\mathrm{MPP}}; \quad V_{\mathrm{PV}} = V_{\mathrm{MPP}} \tag{1}$$

where I_{MPP} and V_{MPP} are the maximum power point current and voltage of the PV module, respectively. Note that the minus sign in the PV current indicates that it is injected (according to the passive sign convention). The equivalent circuit that corresponds to (1) is shown at the top of Fig. 1(a).

The study of the grid-connected inverter (DC/AC) is usually done by using the transformed *Park* variables in the synchronous reference frame. However, the *Ku* transformation in the synchronous reference frame (see (21), Appendix B) is adopted in this study because it provides the complex form of the *direct* and *quadrature* components of the transformed *Park* variables (see (26), Appendix B), thus giving the following single complex equation (assuming passive sign convention)

$$v_{\mathrm{f}} = \left[R_{\mathrm{f}} + L_{\mathrm{f}}\left(\mathrm{d}/\mathrm{d}t + \mathrm{j}\omega\right)\right]i_{\mathrm{f}} + v_{\mathrm{gf}} \tag{2}$$

where v_{f}, v_{gf} and i_{f} are the *forward* components of the transformed *Ku* grid voltage, converter voltage and current, respectively, ω is the grid pulsation, and R_{f} and L_{f} are the filter resistance and inductance, respectively. Note that according to (23) (Appendix B), the transformed *Ku* grid voltage is given by

$$v_{\mathrm{f}} = v_{\mathrm{f}}^{+} + v_{\mathrm{f}}^{-}\mathrm{e}^{-\mathrm{j}2\omega t} = \sqrt{3/2}\,\underline{V}^{+} + \sqrt{3/2}\left(\underline{V}^{-}\right)^{*}\mathrm{e}^{-\mathrm{j}2\omega t} \tag{3}$$

where the superscripts *, + and – stand for the conjugate, *positive*- and *negative*-sequence component, respectively. Note that in steady-state conditions, $\underline{V}^{-}$=0 and $\underline{V}^{+}$ equals the phasor of the phase voltage (V), whereas in fault conditions, $\underline{V}^{+}$ and $\underline{V}^{-}$ are given in Table I for all sag types.

TABLE I
SAGS: TYPES, PHASORS AND SYM. COMPONENTS (ADAPTED FROM [36])

Type	Phasor diagram	Phasor expressions	Sym. components
A	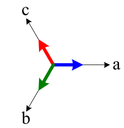	$\underline{V}_a = h\underline{V}$ $\underline{V}_b = -(1/2)h\underline{V} - \mathrm{j}(\sqrt{3}/2)h\underline{V}$ $\underline{V}_c = -(1/2)h\underline{V} + \mathrm{j}(\sqrt{3}/2)h\underline{V}$	$\underline{V}^0 = 0$ $\underline{V}^+ = h\underline{V}$ $\underline{V}^- = 0$
B	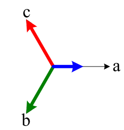	$\underline{V}_a = h\underline{V}$ $\underline{V}_b = -(1/2)\underline{V} - \mathrm{j}(\sqrt{3}/2)\underline{V}$ $\underline{V}_c = -(1/2)\underline{V} + \mathrm{j}(\sqrt{3}/2)\underline{V}$	$\underline{V}^0 = -\frac{1-h}{3}\underline{V}$ $\underline{V}^+ = \frac{2+h}{3}\underline{V}$ $\underline{V}^- = -\frac{1-h}{3}\underline{V}$
C	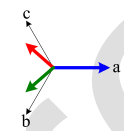	$\underline{V}_a = \underline{V}$ $\underline{V}_b = -(1/2)\underline{V} - \mathrm{j}(\sqrt{3}/2)h\underline{V}$ $\underline{V}_c = -(1/2)\underline{V} + \mathrm{j}(\sqrt{3}/2)h\underline{V}$	$\underline{V}^0 = 0$ $\underline{V}^+ = \frac{1+h}{2}\underline{V}$ $\underline{V}^- = \frac{1-h}{2}\underline{V}$
D	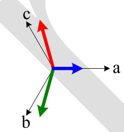	$\underline{V}_a = h\underline{V}$ $\underline{V}_b = -(1/2)h\underline{V} - \mathrm{j}(\sqrt{3}/2)\underline{V}$ $\underline{V}_c = -(1/2)h\underline{V} + \mathrm{j}(\sqrt{3}/2)\underline{V}$	$\underline{V}^0 = 0$ $\underline{V}^+ = \frac{1+h}{2}\underline{V}$ $\underline{V}^- = -\frac{1-h}{2}\underline{V}$
E	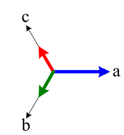	$\underline{V}_a = \underline{V}$ $\underline{V}_b = -(1/2)h\underline{V} - \mathrm{j}(\sqrt{3}/2)h\underline{V}$ $\underline{V}_c = -(1/2)h\underline{V} + \mathrm{j}(\sqrt{3}/2)h\underline{V}$	$\underline{V}^0 = \frac{1-h}{3}\underline{V}$ $\underline{V}^+ = \frac{1+2h}{3}\underline{V}$ $\underline{V}^- = \frac{1-h}{3}\underline{V}$
F	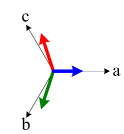	$\underline{V}_a = h\underline{V}$ $\underline{V}_b = -(1/2)h\underline{V} - \mathrm{j}\left[(2+h)/\sqrt{12}\right]\underline{V}$ $\underline{V}_c = -(1/2)h\underline{V} + \mathrm{j}\left[(2+h)/\sqrt{12}\right]\underline{V}$	$\underline{V}^0 = 0$ $\underline{V}^+ = \frac{1+2h}{3}\underline{V}$ $\underline{V}^- = -\frac{1-h}{3}\underline{V}$
G	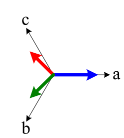	$\underline{V}_a = \left[(2+h)/3\right]\underline{V}$ $\underline{V}_b = -\left[(2+h)/6\right]\underline{V} - \mathrm{j}(\sqrt{3}/2)h\underline{V}$ $\underline{V}_c = -\left[(2+h)/6\right]\underline{V} + \mathrm{j}(\sqrt{3}/2)h\underline{V}$	$\underline{V}^0 = 0$ $\underline{V}^+ = \frac{1+2h}{3}\underline{V}$ $\underline{V}^- = \frac{1-h}{3}\underline{V}$

B. Control of a Grid-Connected PV System

[Case 1: Constant Forward Voltage Control (CFVC)]: The *forward* component of the transformed *Ku* voltage of the converter, v_{gf}, is assumed to be kept constant at its pre-fault steady-state value [29]–[30]. Under these circumstances, (2) is a first-order ordinary differential equation (ODE) with constant coefficients, whose solution during the fault event is

$$i_{\mathrm{f}} = \underline{K}_1\mathrm{e}^{-(R_{\mathrm{f}}/L_{\mathrm{f}})(t-t_{\mathrm{i}})}\mathrm{e}^{-\mathrm{j}\omega(t-t_{\mathrm{i}})} - \underline{K}_2\mathrm{e}^{-\mathrm{j}2\omega t} + \underline{K}_3 \quad (t_{\mathrm{i}} \le t < t_{\mathrm{f}}) \tag{4}$$

where t_{i} and t_{f} are the initial and final time instants, respectively, of the sag duration ($\Delta t = t_{\mathrm{f}} - t_{\mathrm{i}}$), and K_1, K_2 and K_3

are the following complex constants

$$\underline{K}_1 = \frac{v_{\mathrm{f\ st}} - v_{\mathrm{f}}^{+}}{R_{\mathrm{f}} + \mathrm{j}\omega L_{\mathrm{f}}} + \underline{K}_2 \mathrm{e}^{-\mathrm{j}2\omega t_{\mathrm{i}}};\ \underline{K}_2 = -\frac{v_{\mathrm{f}}^{-}}{R_{\mathrm{f}} - \mathrm{j}\omega L_{\mathrm{f}}};\ \underline{K}_3 = \frac{v_{\mathrm{f}}^{+} - v_{\mathrm{gf}}}{R_{\mathrm{f}} + \mathrm{j}\omega L_{\mathrm{f}}} \tag{5}$$

where $v_{\mathrm{f\ st}}$ is the steady-state value of the *forward* grid voltage (see (25), Appendix B). Then, in order to simulate the behavior of a GSC with CFVC strategy it is enough to consider (4)–(5) and replace v_{f}^{+} and v_{f}^{-} by the *positive*- and *negative*-sequence components of voltage sags, according to (3).

Case 2 [Balanced Positive-Sequence Control (BPSC)]: According to the instantaneous power theory (or *p-q* theory) [41], [42] it is possible to obtain the active and reactive powers by means of the *direct* (d) and *quadrature* (q) components of the transformed *Park* variables as

$$\begin{aligned} p(t) &= P + P_{\cos}\cos(2\omega t) + P_{\sin}\sin(2\omega t) \\ q(t) &= Q + Q_{\cos}\cos(2\omega t) + Q_{\sin}\sin(2\omega t) \end{aligned} \tag{6}$$

where P, Q, $P_{\cos}$, $Q_{\cos}$, $P_{\sin}$ and $Q_{\sin}$ are obtained as

$$\begin{aligned} P &= v_{\mathrm{d}}^{+}i_{\mathrm{d}}^{+} + v_{\mathrm{q}}^{+}i_{\mathrm{q}}^{+} + v_{\mathrm{d}}^{-}i_{\mathrm{d}}^{-} + v_{\mathrm{q}}^{-}i_{\mathrm{q}}^{-} & Q &= -v_{\mathrm{d}}^{+}i_{\mathrm{q}}^{+} + v_{\mathrm{q}}^{+}i_{\mathrm{d}}^{+} - v_{\mathrm{d}}^{-}i_{\mathrm{q}}^{-} + v_{\mathrm{q}}^{-}i_{\mathrm{d}}^{-} \\ P_{\cos} &= v_{\mathrm{d}}^{+}i_{\mathrm{d}}^{-} + v_{\mathrm{q}}^{+}i_{\mathrm{q}}^{-} + v_{\mathrm{d}}^{-}i_{\mathrm{d}}^{+} + v_{\mathrm{q}}^{-}i_{\mathrm{q}}^{+} & Q_{\cos} &= -v_{\mathrm{d}}^{+}i_{\mathrm{q}}^{-} + v_{\mathrm{q}}^{+}i_{\mathrm{d}}^{-} - v_{\mathrm{d}}^{-}i_{\mathrm{q}}^{+} + v_{\mathrm{q}}^{-}i_{\mathrm{d}}^{+} \\ P_{\sin} &= v_{\mathrm{d}}^{+}i_{\mathrm{q}}^{-} - v_{\mathrm{q}}^{+}i_{\mathrm{d}}^{-} - v_{\mathrm{d}}^{-}i_{\mathrm{q}}^{+} + v_{\mathrm{q}}^{-}i_{\mathrm{d}}^{+} & Q_{\sin} &= v_{\mathrm{d}}^{+}i_{\mathrm{d}}^{-} + v_{\mathrm{q}}^{+}i_{\mathrm{q}}^{-} - v_{\mathrm{d}}^{-}i_{\mathrm{d}}^{+} - v_{\mathrm{q}}^{-}i_{\mathrm{q}}^{+}. \end{aligned} \tag{7}$$

The following assumptions are made: no *negative*-sequence current is injected during the sag (balanced *positive*-sequence control or BPSC [6]), a phase-locked loop (PLL) [43] is used to obtain the phase angle while synchronizing with the *positive*-sequence component of the grid voltage, v_{d}^{+}, and the inverter works with unitary power factor. Then, from (6)–(7) the reference values of the transformed *Park* currents are

$$\begin{aligned} p(t) &= P_{\mathrm{ref}} = v_{\mathrm{d}}^{+}i_{\mathrm{d\ ref}}^{+} &&\rightarrow i_{\mathrm{d\ ref}}^{+} = P_{\mathrm{ref}}\big/v_{\mathrm{d}}^{+};\ i_{\mathrm{d\ ref}}^{-} = 0 \\ q(t) &= Q_{\mathrm{ref}} = 0 = -v_{\mathrm{d}}^{+}i_{\mathrm{q\ ref}}^{+} &&\rightarrow i_{\mathrm{q\ ref}}^{+} = 0;\ i_{\mathrm{q\ ref}}^{-} = 0. \end{aligned} \tag{8}$$

The current reference values (8) are the inputs of a dual current control (DCC) [44] that controls both *positive*- and *negative*-sequence currents independently. If (26) (Appendix B) is used in (8), then the *forward positive*- and *negative*-sequence components of the *Ku* reference currents are

$$\begin{aligned} &\mathrm{Re}\{i_{\mathrm{f\ ref}}^{+}\} = \frac{P_{\mathrm{ref}}}{2Re\{v_{\mathrm{f}}^{+}\}};\ \mathrm{Im}\{i_{\mathrm{f\ ref}}^{+}\} = 0 \rightarrow i_{\mathrm{f\ ref}}^{+} = \frac{P_{\mathrm{ref}}}{2Re\{v_{\mathrm{f}}^{+}\}} \\ &\mathrm{Re}\{i_{\mathrm{f\ ref}}^{-}\} = 0;\ \mathrm{Im}\{i_{\mathrm{f\ ref}}^{-}\} = 0 \rightarrow i_{\mathrm{f\ ref}}^{-} = 0. \end{aligned} \tag{9}$$

Then, in order to simulate the behavior of a GSC with BPSC strategy, the reference values to be used for a dual current control [44] are given in (9), and the electrical model of (2) has to be used to emulate the dynamics of the GSC under sags.

Case 3 [BPSC with Grid Code Requirements (BPSC-GCR)]: This is the proposed control strategy in this paper, which combines the BPSC [6] (explained in Case 2) plus the grid code requirements imposed by Spanish transmission system operator [11]. The proposed BPSC-GCR control strategy is summarized in the block diagram depicted in Fig. 3 and it is explained below.

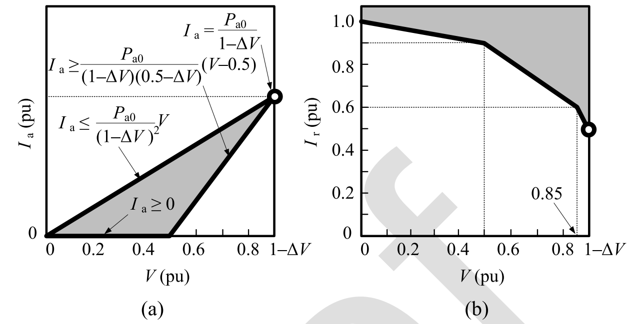

Fig. 2. Spanish grid code used for FRT during voltage sags (adapted from [11]). (a) Active current (I_{a}) injection (the solid line indicates its upper and lower limits), and (b) reactive current (I_{r}) injection (the solid line indicates its minimum requirements). Variables: P_{a0} = pre-fault injected power (per unit value); ΔV = symmetrical voltage range surrounding the rated voltage (around ± 10% for transmission grids [12]). The shaded area corresponds to the possible values to be adopted for the injected currents. The marked points correspond to the active and reactive current limits considering a voltage magnitude V (pu) = 0.9 during the sag.

Firstly, the per unit value of the rms voltage during the fault is obtained as

$$V(\mathrm{pu}) = \left[\sqrt{\left(V_{\mathrm{a}}^2 + V_{\mathrm{b}}^2 + V_{\mathrm{c}}^2\right)\big/3}\,\right]\Big/V \tag{10}$$

where V is the modulus (rms voltage) of the pre-fault phase voltage, and V_{a}, V_{b} and V_{c} are the moduli of the faulted phase voltages, which can be obtained by means of the phasor expressions shown in Table I, according to the sag type.

Secondly, (10) is used in Fig. 2 to determine the values of the active current (I_{a}) and reactive current (I_{r}) to be injected by the inverter during the fault. If the inverter current limit is exceeded, more priority should be given for the reactive current

$$I_{\mathrm{a\ lim}} = \sqrt{I_{\mathrm{GSC\ max}}^2 - I_{\mathrm{r}}^2}. \tag{11}$$

Thirdly, I_{a} and I_{r} are used to obtain the *forward positive*-component of the transformed *Ku* current, while its *negative*-sequence component is set to zero (BPSC strategy), so

$$i_{\mathrm{f\ ref}}^{+} = (I_{\mathrm{a}} + \mathrm{j}I_{\mathrm{r}})\big/\sqrt{2};\quad i_{\mathrm{f\ ref}}^{-} = 0. \tag{12}$$

Then, a current loop controls independently the *positive*-sequence and the *negative*-sequence components of the injected current, in the same way as a dual current control does [44], but considering the complex form of the transformed *Park* currents, i.e., the *forward* component of the transformed *Ku* injected current (i_{f}^{+} and i_{f}^{-}, respectively). The K_{p} and K_{i} parameters of the PI controllers have been obtained by equaling the denominator's coefficients of the closed-loop transfer function (system plus PI controller) with the characteristic equation of a second order transfer function, using a nominal closed-loop natural frequency of 22.6 rads^{-1} and an overshoot of 0.4. A PLL has been used to obtain the angle of the grid voltages, Ψ, which is the transformation angle for the *Ku* transformation (see Appendix B). Note that the angles Ψ and $-\Psi$ are used to obtain the *positive*-sequence and the *negative*-sequence components of the transformed *Ku* variables, respectively.

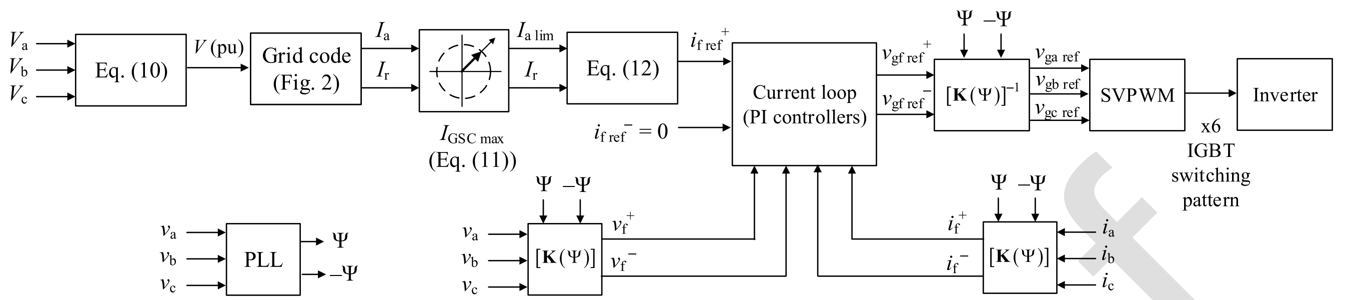

Fig. 3. Proposed balanced *positive*-sequence control with grid code requirements (BPSC-GCR) strategy for three-phase grid-connected inverters under voltage sags. Acronyms: PLL = phase-locked loop; SVPWM = space vector pulse-width modulation.

Finally, the outputs of the current control loop are the *positive*-sequence and the *negative*-sequence components of the *forward* component of the transformed *Ku* reference voltage ($v_{\mathrm{gf\ ref}}{}^{+}$ and $v_{\mathrm{gf\ ref}}{}^{-}$, respectively). Then, by applying the inverse *Ku* transformation (see Appendix B), the abc components of the reference voltages are obtained ($v_{\mathrm{gabc\ ref}}$), which are used in a space vector pulse-width modulation (SVPWM) technique in order to obtain the switching pattern for the inverter's 6 IGBTs.

Lastly, it should be noted that the proposed methodology, which is summarized in Fig. 3, is valid for any grid code. The only difference lies in the active and reactive current limits, which are imposed by each grid code (in this paper they have been obtained from the Spanish grid code, shown in Fig. 2).

IV. Grid-Connected DFIG-Based WT

A. Analytical Model of a DFIG-Based WT

Fig. 1(b) shows the electrical scheme of a DFIG-based WT, which consists of a three-phase wound-rotor induction machine whose stator is directly connected to the grid and its rotor is connected to the grid through a back-to-back converter, where a rotor-side converter (RSC) is connected to a GSC through a DC link. The rotor of the DFIG is connected to a three-bladed wind turbine through a gearbox, which adapts the low-speed shaft (blades) with the high-speed shaft (DFIG).

The electrical equations of a three-phase DFIG written in *Ku* components assuming motor sign convention are

$$\begin{aligned} v_{\mathrm{sf}} &= \left[R_{\mathrm{s}} + L_{\mathrm{s}}\left(\mathrm{d}/\mathrm{d}t + \mathrm{j}\omega_{\mathrm{s}}\right)\right] i_{\mathrm{sf}} + M\left(\mathrm{d}/\mathrm{d}t + \mathrm{j}\omega_{\mathrm{s}}\right) i_{\mathrm{rf}} \\ v_{\mathrm{rf}} &= \left[R_{\mathrm{r}} + L_{\mathrm{r}}\left(\mathrm{d}/\mathrm{d}t + \mathrm{j}s\omega_{\mathrm{s}}\right)\right] i_{\mathrm{rf}} + M\left(\mathrm{d}/\mathrm{d}t + \mathrm{j}s\omega_{\mathrm{s}}\right) i_{\mathrm{sf}} \end{aligned} \tag{13}$$

where v_{sf} and v_{rf} are the *forward* components of the transformed *Ku* stator and rotor voltages, respectively, i_{sf} and i_{rf} are the *forward* components of the transformed *Ku* stator and rotor currents, respectively, R_{s} and R_{r} are the per-phase stator and rotor resistances, respectively, L_{s} and L_{r} are the per-phase inductances of the stator and rotor windings, respectively, M is the magnetizing inductance, ω_{s} is the pulsation of the stator voltages and $s = (\omega_{\mathrm{s}} - p\omega_{\mathrm{m}})/\omega_{\mathrm{s}}$ is the mechanical slip (where p = number of pole pairs and ω_{m} = DFIG mechanical speed). The equivalent circuit of (13) is shown at the top of Fig. 1(b).

B. Control of a DFIG-Based WT

An MPPT algorithm is used to obtain the optimum speed to which the DFIG should rotate in order to get the maximum power for a given wind speed [45]. Moreover, a pitch actuator controls the aerodynamic power of the WT when operating under high-wind-speed regions [46].

The GSC is controlled in order to inject the active and reactive currents according to the grid code requirements (see Section III-B, Case 3, for more details).

The RSC is controlled by means of a vector control in the synchronous reference frame, where the *direct* and *quadrature* components of the transformed *Park* rotor current are used to control the reactive power (unitary power factor) and the speed/torque (whose reference value is given by the MPPT algorithm), respectively [47]. In this paper, the control of the RSC is done with the transformed *Ku* variables in the synchronous reference frame (Appendix B).

The following assumptions are made:

1) Pre-fault steady-state conditions: the DFIG-based WT delivers to the grid its rated power, which corresponds to the rated wind speed. As a result, the DFIG slip has its rated value.

2) Simulated sags: short durations (milliseconds). Then, due to the high inertia of the system, the mechanical control cannot change the pitch angle during the event and the mechanical speed is constant (its value corresponds to the rated slip).

3) Control: it keeps constant the transformed *Ku* rotor current in the synchronous reference frame at its pre-fault steady-state value during all the entire event [22]–[24].

It should be noted that both mechanical slip and transformed *Ku* rotor current are constant, so (13) is a first-order ODE with constant coefficients, whose solution during the fault is

$$i_{\mathrm{sf}} = \underline{C}_1\, \mathrm{e}^{-(R_{\mathrm{s}}/L_{\mathrm{s}})(t-t_{\mathrm{i}})} \mathrm{e}^{-\mathrm{j}\omega_{\mathrm{s}}(t-t_{\mathrm{i}})} + \underline{C}_2\, \mathrm{e}^{-\mathrm{j}2\omega_{\mathrm{s}}t} + \underline{C}_3 (t_{\mathrm{i}} \le t \le t_{\mathrm{f}}) \tag{14}$$

where t_{i} and t_{f} are the initial and final time instants, respectively, of the sag duration ($\Delta t = t_{\mathrm{f}} - t_{\mathrm{i}}$), and C_1, C_2 and C_3 are the following complex constants

$$\underline{C}_1 = \frac{v_{\mathrm{sfst}} - v_{\mathrm{sf}}^{+}}{R_{\mathrm{s}} + \mathrm{j}\omega_{\mathrm{s}} L_{\mathrm{s}}} - \underline{C}_2 \mathrm{e}^{-\mathrm{j}2\omega_{\mathrm{s}} t_{\mathrm{i}}};\ \underline{C}_2 = \frac{v_{\mathrm{sf}}^{-}}{R_{\mathrm{s}} - \mathrm{j}\omega_{\mathrm{s}} L_{\mathrm{s}}};\ \underline{C}_3 = \frac{v_{\mathrm{sf}}^{+} - \mathrm{j}\omega_{\mathrm{s}} M i_{\mathrm{rf}}}{R_{\mathrm{s}} + \mathrm{j}\omega_{\mathrm{s}} L_{\mathrm{s}}} \tag{15}$$

where $v_{\mathrm{sf}}{}^{+}$ and $v_{\mathrm{sf}}{}^{-}$ are the *forward* stator voltage (grid voltage) related to its symmetrical components (3) and $v_{\mathrm{sf\ st}}$ is the steady-state value of the *forward* stator voltage (see (25), Appendix B).

TABLE II
CONTROLLABILITY OF GSC AND RSC OF RES-BASED DPGSs UNDER SAGS

		Fault Ride-Through Capability? (■ = Yes, □ = No)									
		Sag Duration (cycles)					Sag Depth (pu)				
		5	5.5	6	6.5	7	0.5	0.6	0.7	0.8	0.9
GSC	CFVC	■	□	■	□	■	□	□	□	□	■
	BPSC	■	■	■	■	■	□	□	□	□	■
	BPSC-GCR	■	■	■	■	■	□	■	■	■	■
RSC	6 MW	■	□	■	□	■	□	□	□	■	■
	2 MW	□	□	□	□	□	□	□	□	□	□
	7.5 kW	■	□	■	□	■	□	□	□	□	■

Acronyms: BPSC = balanced *positive*-sequence control, CFVC = constant *forward* voltage control, GCR = grid code requirements, GSC = grid-side converter, RSC = rotor-side converter.

Finally, if $\mathrm{d}i_{\mathrm{sf}}/\mathrm{d}t$ from the first equation of (13) is substituted in its second equation and given that $\mathrm{d}i_{\mathrm{rf}}/\mathrm{d}t = 0$ (because the control imposes $i_{\mathrm{rf}} = \text{constant}$), then the *forward* component of the transformed *Ku* rotor voltage is

$$v_{\mathrm{rf}} = \frac{M}{L_{\mathrm{s}}} v_{\mathrm{sf}} + M\left[-\frac{R_{\mathrm{s}}}{L_{\mathrm{s}}} + \mathrm{j}\omega_{\mathrm{s}}(s-1)\right] i_{\mathrm{sf}} + \left[R_{\mathrm{r}} + \mathrm{j}\omega_{\mathrm{s}}\left(sL_{\mathrm{r}} - \frac{M^2}{L_{\mathrm{s}}}\right)\right] i_{\mathrm{rf}} \tag{16}$$

where v_{sf} is obtained according to (3), i_{sf} is obtained according to (14)–(15) and i_{rf} =constant at its pre-fault steady-state value.

Then, in order to simulate the behavior of DFIG-based WTs under voltage sags with the control strategy of constant transformed rotor current [22]–[24], equations (14)–(16) have to be used, which correspond to the dynamics of transformed stator current and transformed rotor voltage, respectively.

V. SIMULATION RESULTS

A. GSC Controllability (PV System) Under Sags

The GSC (PV system) is controlled by means of the three control strategies explained in Section III-B. The chosen variable to analyze the controllability of GSC (PV system) under sags is the maximum per-unit value of the injected current

$$i_{\mathrm{peakpu}} = \frac{\max\{|i_{\mathrm{f}}(t)|\}}{\sqrt{3/2}I_{\mathrm{n}}} = \frac{\max\{|i_{\mathrm{a}}(t)|, |i_{\mathrm{b}}(t)|, |i_{\mathrm{c}}(t)|\}}{\sqrt{2}I_{\mathrm{n}}} \tag{17}$$

where I_{n} is the rated current and $i_{\mathrm{f}}(t)$ is the *forward* component of the transformed injected current, given by (2) depending on the adopted control strategy. The peak current of the converter contribution is $\sqrt{2}$ times the RMS value [48]. In order to consider a more restrictive approach, the current limit of the GSC of the PV system is set to 1.2 times the rated current:

$$I_{\mathrm{GSC\ max}} = 1.2 I_{\mathrm{n}}. \tag{18}$$

Fig. 4(a) and Fig. 4(b) show the MATLAB simulation results for the sag duration influence and sag depth influence, respectively, on the peak current of a GSC of PV systems, whose parameters are shown in Appendix A. Given that most of faults in transmission systems are cleared around 100 ms [49], the simulated sag durations [Fig. 4(a)] are defined between 5 cycles to 7 cycles (i.e., from 100 ms to 140 ms, assuming a grid frequency of 50 Hz). Moreover, the sag depths have been simulated from 0.5 to 0.9 pu [Fig. 4(b)] because most of sag depths in high voltage and mid voltage sites occur within this range [49]. The results are summarized in Table II and it can be concluded that BPSC-GCR is the most suitable control for GSCs of PV systems because $i_{\mathrm{peak}} \leq I_{\mathrm{GSC\ max}}$ for most sag durations and depths. In other words, BPSC-GCR method ensures FRT for GSCs of PV systems, while the other analyzed controls not. It is also observed from Fig. 4(a)–(b) results that balanced sags (A) are more severe than unbalanced sags (B…G) because the peak value of the injected current is higher when the GSC of PV systems operates under sag type A.

Finally, it should be noted that the zoomed points marked Fig. 4(a) and Fig. 4(b) correspond to the peak current values for sag depth $h = 0.9$ and sag duration $\Delta t = 5$ cycles. These peak values are consistent with the peak current values of the experimental results marked in Fig. 7(a) and Fig. 7(b) for BPSC and BPSC-GCR control techniques, respectively.

B. RSC Controllability (DFIG-Based WT) Under Sags

The RSC (DFIG-based WT) is controlled according to the control strategy explained in Section IV-B. The chosen variable to analyze the controllability of RSC of DFIG-based WTs under sags is the maximum per-unit value of the DFIG rotor voltage

$$v_{\mathrm{r\ peak\ pu}} = \frac{\max\{|v_{\mathrm{rf}}(t)|\}}{\sqrt{3/2}V_{\mathrm{n}}} = \frac{\max\{|v_{\mathrm{ra}}(t)|, |v_{\mathrm{rb}}(t)|, |v_{\mathrm{rc}}(t)|\}}{\sqrt{2}V_{\mathrm{n}}} \tag{19}$$

where V_{n} is the rated voltage and $v_{\mathrm{rf}}(t)$ is the *forward* component of the transformed rotor voltage, given by (16). It should be noted that the RSC of a DFIG is designed to handle the slip power, i.e., between 20% and 30% of the rated power [50]. As a result, the voltage limit of the RSC of DFIG-based WTs is

$$V_{\mathrm{RSC\ max}} = 0.3 V_{\mathrm{n}}. \tag{20}$$

Fig. 4(c) and Fig. 4(d) show the MATLAB simulation results for the sag duration influence and sag depth influence, respectively, on the peak rotor voltage of different-sized DFIG-based WTs, whose parameters are shown in Appendix A. The same sag durations and depths as in the previous subsection have been considered for the simulations. It is observed that a DFIG under sag type A exhibits higher values of rotor voltage peak than when it operates under unbalanced sags (types B…G). Finally, it should be noted that the effects of sag types E and G on the rotor voltage peak are the same: this is because the DFIG stator windings are connected either in isolated star or in delta, so there is no *zero*-sequence component. Therefore, according to Table I, both sag types have the same symmetrical components.

C. Remarks on the Controllability of RES-Based DPGSs

The FRT capability of the studied RES-based DPGSs under voltage sags is summarized in Table II. Two main conclusions

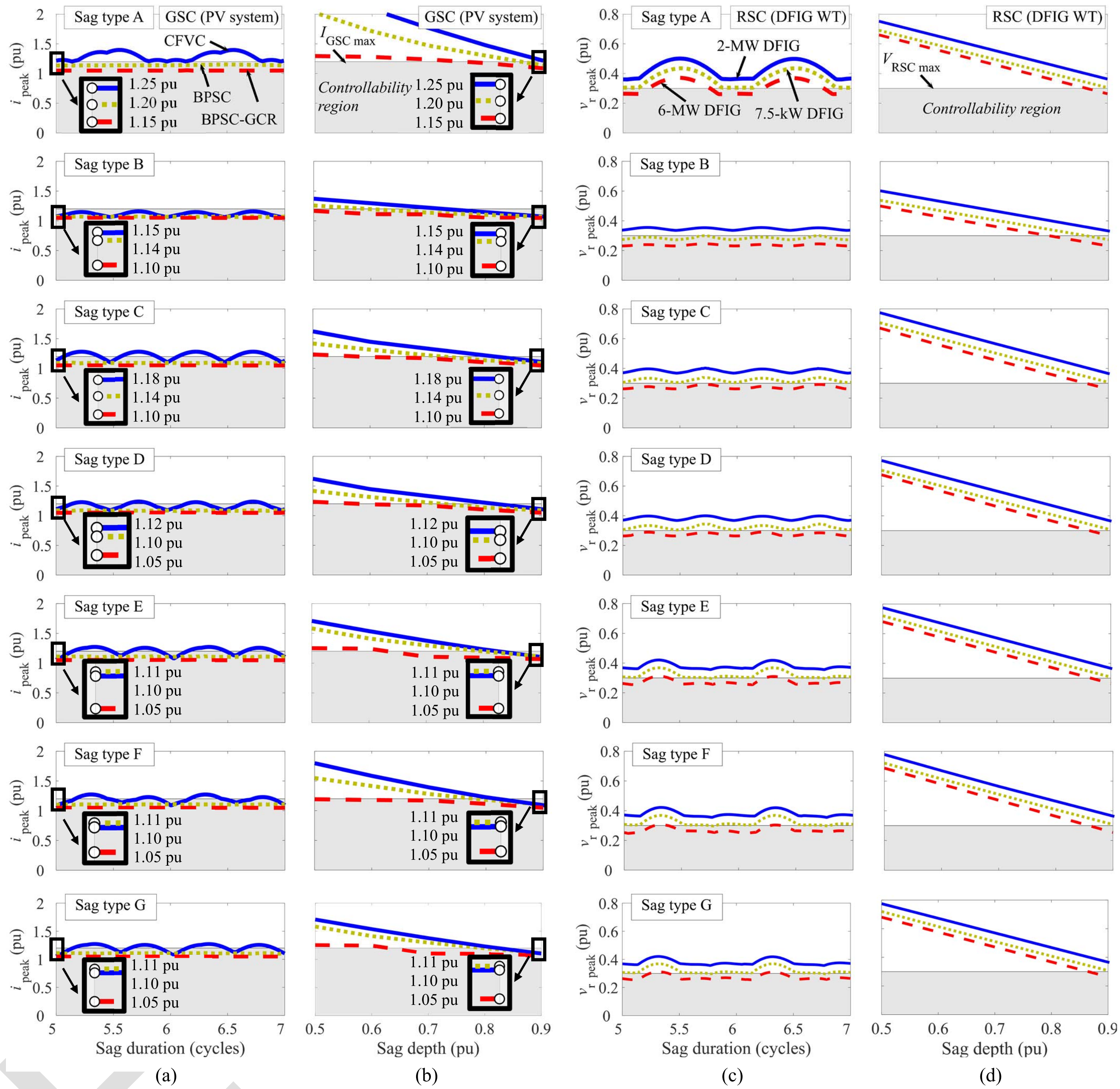

Fig. 4. Sag parameters influence on the controllability of RES-based DPGSs. (a) Sag duration influence on the GSC (PV system), (b) sag depth influence on the GSC (PV system), (c) sag duration influence on the RSC (DFIG-based WT), and (d) sag depth influence on the RSC (DFIG-based WT). Sag characteristics for sag duration influence: $h = 0.9$, $\Delta t = 5$ cycles…7 cycles and $\psi = 80°$. Sag characteristics for sag depth influence: $h = 0.5 \ldots 0.9$, $\Delta t = 5$ cycles and $\psi = 80°$). Acronyms: BPSC = balanced *positive*-sequence control; CFVC = constant *forward* voltage control; GCR = grid code requirements; GSC = grid-side converter; RSC = rotor-side converter. The shaded area corresponds to the controllability region. The zoomed points in (a) and (b) correspond to the peak current values for sag depth $h = 0.9$ and sag duration $\Delta t = 5$ cycles, which are consistent with the peak current values of the experimental results marked in Fig. 7(a) and Fig. 7(b) for BPSC and BPSC-GCR control techniques, respectively.

can be drawn from this table: on the one hand, the effects of sag durations with uneven cycles are the most severe and, on the other hand, different-sized units exhibit dissimilar behavior under the same sag parameters. All of this is discussed below.

It is interesting to note from the results shown in Fig. 4(a) and Fig. 4(c) that sag durations with uneven cycles (e.g., 5.5 cycles) cause more severe effects on the current than sag durations with n cycles. This is explained in Fig. 5(a) and Fig. 5(b) considering a 2-MW DFIG-based WT under symmetrical sags with two different sag durations ($\Delta t = 5$ cycles and $\Delta t = 5.5$ cycles, respectively). Note from Fig. 5(a) that in the complex plane, when the sag ends (after 5 cycles) the *forward* component of the transformed *Ku* stator current (i_{sf}, in the complex plane) is near the pre-sag value, so after voltage recovery the stator current exhibits no peak, as can be seen in the time evolution of the abc components of this current. However, in Fig. 5(b) it is observed that once the sag ends (after 5.5 cycles), the value of i_{sf} is further from its pre-sag value, soit means that after voltage recovery, the locus of i_{sf} is a spiral with a higher diameter. As a result, the time evolution

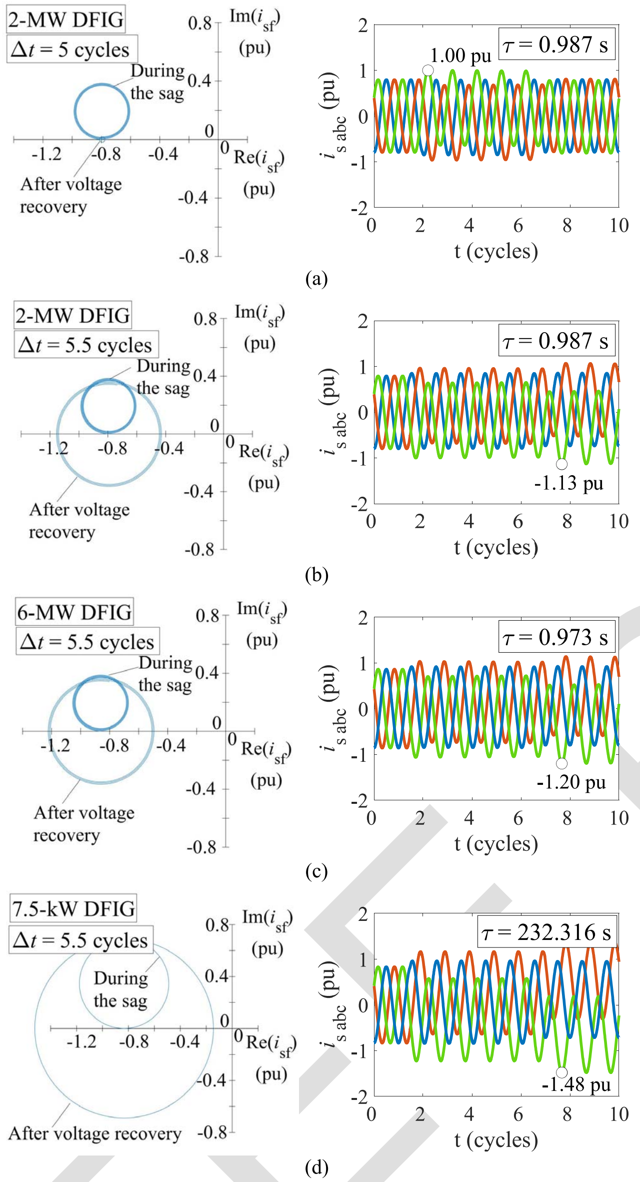

Fig. 5. DFIG stator current (real part vs. imaginary of the *forward* component of the transformed *Ku* stator current and time evolution of the abc components) under symmetrical voltage sags (sag type A) with sag parameters: $h = 0.4$ and $\psi = 80°$. (a) 2 MW DFIG-based WT under sag type A with duration $\Delta t = 5$ cycles, (b) 2-MW DFIG under sag type A with duration $\Delta t = 5.5$ cycles, (c) 6-MW DFIG under sag type A with duration $\Delta t = 5.5$ cycles, and (d) 7.5-kW DFIG under sag type A with duration $\Delta t = 5.5$ cycles.

of the abc components of the stator current exhibits higher peaks than in the case of sag type with 5 cycles. This effect has also been noticed in the authors' previous works [22]–[24].

On the other hand, the differences in the controllability of the studied WT units can be explained by means of the time constant $\tau = L_s/R_s$ that appears in the exponential term $e^{-t/\tau}$ in (14). According to the DFIG-based WT parameters shown in Appendix A, the time constant for all the studied units are: $\tau = 0.987$ s for the 2-MW DFIG, $\tau = 0.973$ s for the 6-MW DFIG and $\tau = 232.316$ s for the 7.5-kW DFIG (note that this value is very high due to the small value of the stator resistance for small-sized units). As a result, the different time constants cause dissimilar behavior during the sag and after voltage recovery for the studied DFIG units.

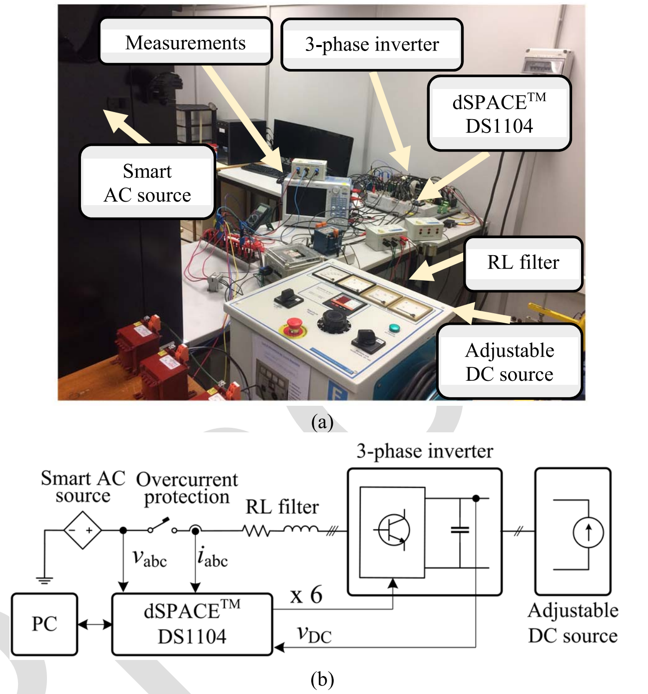

Fig. 6. Experimental setup of the tested 10-kVA three-phase inverter. (a) Real setup, and (b) electrical scheme.

The aforementioned effect is proved by the results shown in Fig. 5(b) (2-MW DFIG), Fig. 5(c) (6-MW DFIG) and Fig. 5(d) (7.5-kW DFIG), where all the DFIG units have been simulated under symmetrical sags (sag type A) with the same sag depth ($h = 0.4$) and the same sag duration ($\Delta t = 5.5$ cycles). In the complex plane it is observed that the 2-MW and the 6-MW DFIGs behave quite similarly under sags (showing a spiral waveform during the sag and after voltage recovery), because their time constants are similar. However, note that the 7.5-kW DFIG has almost no damping in the stator current (due to the large value of its time constant), so the stator current in the complex plane exhibits a circular shape, rather than an exponential one. All of this cause dissimilar time evolution in the abc components of the stator current for the different-sized DFIG units: indeed, it is observed that the peak values of the stator current are different for all the DFIGs, and the most severe case (the highest peak value) is obtained for the smallest DFIG unit, because its resistance is very small, so its time constant is large and there is scarcely no damping effect during the sag and after voltage recovery. To sum up, although a DFIG-based WT can achieve FRT when subject to a specific sag, it may not be controllable for another DFIG-based WT unit operating under the same sag conditions, due to their different time constants. Therefore, special care should be taken when extrapolating the results of a small-size DFIG to explain the behavior of a larger unit.

VI. Experimental Results

A real 10-kVA three-phase inverter of CINERGIA, whose parameters are shown in Appendix A, has been tested under voltage sags generated by a 4.5-kVA three-phase Pacific Power

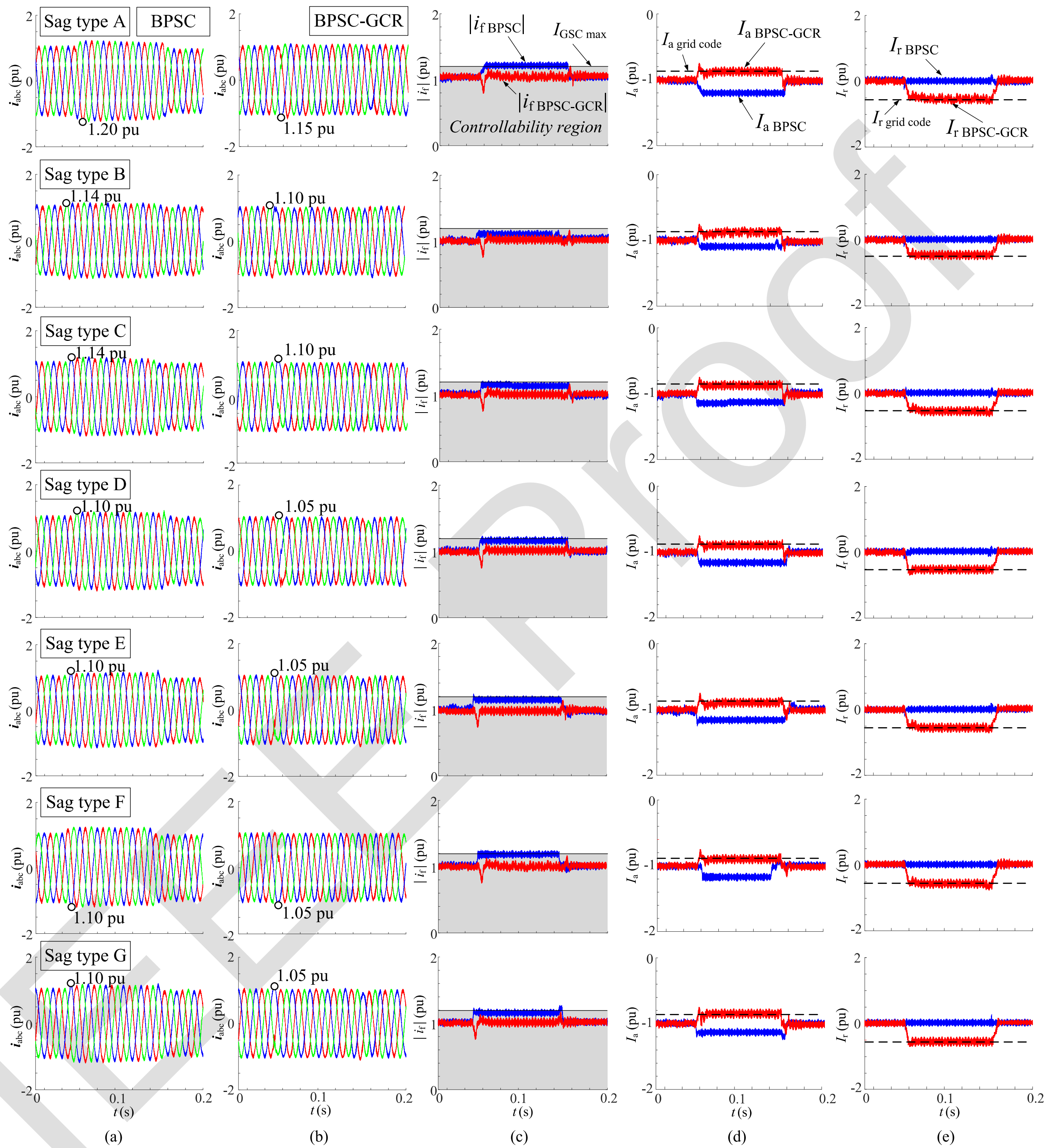

Fig. 7. Experimental results of the tested 10-kVA three-phase inverter connected to a sag generator. (a) abc components of the injected current with BPSC strategy, (b) abc components of the injected current with the proposed BPSC-GCR strategy, (c) modulus of the *forward* component of the *Ku* transformed injected current with both BPSC and BPSC-GCR strategies, (d) injected active current with both BPSC and BPSC-GCR strategies, and (e) injected reactive current with both BPSC and BPSC-GCR strategies, Sag characteristics: $h = 0.9$, $\Delta t = 5$ cycles and $\psi = 80°$. Acronyms: BPSC = balanced *positive*-sequence control; GCR = grid code requirements. The shaded area corresponds to the controllability region. The points marked in (a) and (b) correspond to the peak current values for sag depth $h = 0.9$ and sag duration $\Delta t = 5$ cycles, which are the same as the peak current values of the simulation results zoomed in Fig. 4(a) and Fig. 4(b) for BPSC and BPSC-GCR control techniques, respectively.

Source, with model 345AMXT, which emulates the faulty grid. Data acquisition and switching pattern sending to the IGBTs has been done by means of a dSPACE DS1104. Fig. 6(a) shows a photograph of the experimental setup and Fig. 6(b) shows its electrical scheme.

Fig. 7 shows the comparison between the experimental results of the tested three-phase inverter under all voltage sag types using BPSC strategy and the proposed BPSC-GCR strategy. Note that the CFVC strategy has not been compared experimentally due to its worst

TABLE III
SUMMARY OF EXPERIMENTAL RESULTS FOR THE TESTED INVERTER

Sag Type	Grid Code Requirements*		Grid Code Compliance? (■ = Yes, □ = No)		Peak Current (in pu)		FRT Capability? (■ = Yes, □ = No)	
	$I_{a\ grid\ code}$ (pu)	$I_{r\ grid\ code}$ (pu)	BPSC	BPSC-GCR	BPSC	BPSC-GCR	BPSC	BPSC-GCR
A	– 0.83	– 0.56	□	■	1.20	1.15	□	■
B	– 0.87	– 0.50	□	■	1.14	1.10	■	■
C	– 0.86	– 0.51	□	■	1.14	1.10	■	■
D	– 0.86	– 0.51	□	■	1.10	1.05	■	■
E	– 0.85	– 0.53	□	■	1.10	1.05	■	■
F	– 0.85	– 0.53	□	■	1.10	1.05	■	■
G	– 0.85	– 0.53	□	■	1.10	1.05	■	■

* The grid code requirements correspond to the tested sag types with $h = 0.9$. The negative values mean that currents are injected by the inverter, according to the passive sign convention (Fig. 1).

Acronyms: BPSC = balanced *positive*-sequence control, GCR = grid code requirements.

response under voltage sags (as explained in the previous section).

Fig. 7(a) and Fig. 7(b) show the time evolution of the abc components of the injected current by the tested three-phase inverter under all voltage sag types with BPSC strategy and BPSC-GCR strategy, respectively. It is observed that the BPSC-GCR strategy smooths the voltage sag effects on the three-phase inverter, since the peak value of the abc injected currents has a lower value than the peak current of the abc injected current with BPSC for all sag types.

Fig. 7(c) shows the modulus of the *forward* component of the transformed *Ku* current injected by the tested three-phase inverter under all voltage sag types with BPSC strategy and the proposed BPSC-GCR strategy. It is observed that the proposed BPSC-GCR strategy ensures FRT because the modulus of the transformed current is lower than the inverter's current limit ($|i_f| \leq I_{GSC\ max}$) for the tested balanced and unbalanced sags. Note that BPSC strategy cannot ensure FRT for all the tested sags.

Fig. 7(d) and Fig. 7(e) show the time evolution of the active current, I_a, and reactive current, I_r, respectively, injected by the tested three-phase inverter under all voltage sag types with BPSC strategy and the proposed BPSC-GCR strategy. Note that I_a and I_r are related to the real and imaginary parts of the measured transformed *Ku* injected current, as seen in (12). It is observed that the proposed BPSC-GCR control strategy meets grid code requirements because I_a and I_r follow active and reactive current values demanded by the grid code during the sag ($I_{a\,grid\ code}$ and $I_{r\ grid\ code}$, respectively). Note that $I_{a\ grid\,code}$ and $I_{r\ grid\ code}$ have been obtained from Fig. 2 with $h = 0.9$ (which is the sag depth of the tested sags in the lab) and their values are shown in Table III for all sag types. Note also that BPSC strategy does not meet grid code requirements, because during the sag both injected active and reactive currents do not follow the demanded currents by the grid code (this is especially critical for reactive current, because there is no reactive current injection during the sag with BPSC strategy).

Finally, all the experimental results are summarized in Table III. Judging by the experimental results, it can be concluded that BPSC-GCR is the most suitable control strategy for grid-connected inverters under voltage sags because it reduces the peak current values (thus making it possible to achieve FRT) and it meets grid code requirements.

TABLE IV
CHARACTERISTICS OF THE SIMULATED PV SYSTEM AND TESTED SYSTEM

Simulated PV System							
Rated Values					Parameters in pu		
Generation		DC	AC		($S_b = P_n$, $V_b = V_n$, $f_b = f_n$)		
P_n	$\cos(\varphi_n)$	V_{dc}	V_n (phase)	f_n	C	R_f	L_f
50 kW	1	1000 V	230 V	50 Hz	18.095	$3.125 \cdot 10^{-4}$	0.4810
Tested System (Experimental Setup)							
Rated Values					Parameters in pu		
Generation		DC	AC		($S_b = P_n$, $V_b = V_n$, $f_b = f_n$)		
P_n	$\cos(\varphi_n)$	V_{dc}	V_n (phase)	f_n	C	R_f	L_f
0.6 kW	1	260 V	74.5 V	50 Hz	2.9642	0.0216	0.3396

VII. CONCLUSION

This paper has shown the importance of meeting grid code requirements for RES-based DPGSs operating in a faulty grid with both balanced and unbalanced conditions, while ensuring no to exceed the voltage and current limits of power converters. It should be noted that grid codes usually consider balanced grid faults, but most of grid faults are unbalanced. What is more, this paper has shown that unsymmetrical sags whose durations are different from n cycles may cause worse effects on RES-based DPGSs than symmetrical sags whose durations equal n cycles. Moreover, this paper has analyzed the controllability of grid-connected RES-based DPGSs when operating under both balanced and unbalanced voltage sags. Analytical models for a PV system and a DFIG-based WT have been given in the complex form of the *Park* variables and exhaustive simulations considering all sag types with a large range of durations and depths have been carried out. Converter limits have been considered to analyze the situations in which the GSC (PV system) and RSC (DFIG-based WT) can be controlled. The simulations have revealed that the proposed balanced *positive*-sequence control with the grid code requirements (BPSC-GCR) is the optimum control strategy for GSCs of PV systems because it ensures FRT for all sag types with most durations and depths and it meets grid code requirements, which has been corroborated by experimental results. Finally, the authors recommend that similar studies should be carried out in order to face up with the new power system scenario, where it is expected a noticeable increase in the grid penetration of RES-based DPGSs to achieve the goal of a decarbonized society.

APPENDIX A
PARAMETERS OF THE STUDIED RES-BASED DPGSs

Table IV and Table V show the parameters of the studied PV systems and DFIG-based WTs, respectively.

TABLE V
CHARACTERISTICS OF THE SIMULATED DFIGs

DFIG SIZE	RATED VALUES					POLE PAIRS
	P_n	V_n (phase)	f_n	$\omega_{m\,n}$	s_n	p
Offshore [51]	6 MW	2300 V	50 Hz	1170 rpm	– 0.17	3
Onshore [52]	2 MW	400 V	50 Hz	1900 rpm	– 0.27	2
Setup [26]	7.5 kW	220 V	50 Hz	1800 rpm	– 0.20	2
PARAMETERS IN PU ($S_b = P_n$, $V_b = V_n$, $f_b = f_n$)						
	R_s	R_r	L_{sl}	L_{rl}	M	
Offshore [51]	0.0101	0.0097	0.0273	0.0257	3.0522	
Onshore [52]	0.01	0.01	0.10	0.08	3.00	
Setup [26]	$2.399{\cdot}10^{-5}$	$2.457{\cdot}10^{-5}$	0.0641	0.0641	1.6872	

APPENDIX B
Ku TRANSFORMATION

The *Ku* transformation is defined in [53]. Its power-invariant (or normalized form) is

$$[\mathbf{K}(\Psi)] = \frac{1}{\sqrt{3}}\begin{bmatrix} 1 & 1 & 1 \\ e^{-j\Psi} & ae^{-j\Psi} & a^2e^{-j\Psi} \\ e^{j\Psi} & a^2e^{j\Psi} & ae^{j\Psi} \end{bmatrix}$$
$$[\mathbf{K}(\Psi)]^{-1} = [\mathbf{K}(\Psi)]^{T*}; \quad a = e^{j2\pi/3}$$
$$[\mathbf{x_{0fb}}] = [\mathbf{K}(\Psi)][\mathbf{x_{abc}}]; \quad [\mathbf{x_{abc}}] = [\mathbf{K}(\Psi)]^{-1}[\mathbf{x_{0fb}}] \tag{21}$$

where the subscripts abc stand for the three-phase components of a given variable x, the subscripts 0fb stand for the zero, *forward* and *backward* components of the transformed *Ku* variable, Ψ is the transformation angle, which in the synchronous reference frame corresponds to $\Psi = \omega t$ for grid or stator variables and to $\Psi = s\omega t$ for rotor variables (assuming constant speed and zero mechanical angle at $t = 0$), with ω being the pulsation of grid voltages and s being the mechanical slip. Note that backward component equals the complex conjugate of *forward* component, so only the latter needs to be considered.

An unbalanced 3-phase system can be written with the following phasor expressions and time expressions

$$\underline{X}_i = X_i e^{j\varphi_{Xi}} \rightarrow v_i = \sqrt{2}X_i\cos(\omega t + \varphi_{Xi}); \quad i = a, b, c \tag{22}$$

where X_i and φ_{Xi} are the rms values (moduli) and the angles, respectively, of the abc phase components of the studied variable X. If the *Ku* transformation (21) with $\Psi = \omega t$ is applied in (22) and the trigonometric relation $\cos(\alpha) = (e^{j\alpha} + e^{-j\alpha})/2$ is used, then the *forward* component yields

$$x_f = x_f^+ + x_f^- e^{-j2\omega t} \tag{23}$$
$$x_f^+ = \frac{1}{\sqrt{6}}(X_a e^{j\varphi_{Xa}} + aX_b e^{j\varphi_{Xb}} + a^2X_c e^{j\varphi_{Xc}}) = \sqrt{\frac{3}{2}}\underline{X}^+$$
$$x_f^- = \frac{1}{\sqrt{6}}(X_a e^{-j\varphi_{Xa}} + aX_b e^{-j\varphi_{Xb}} + a^2X_c e^{-j\varphi_{Xc}}) = \sqrt{\frac{3}{2}}\left(\underline{X}^-\right)^* \tag{24}$$

with X^+ and X^- being the *positive*- and the *negative*-sequence components, respectively. Note that for balanced three-phase systems, e.g., in the pre-fault steady state conditions or under balanced faults (sag type A), the *negative* sequence component is zero (see Table I), so (23) results in

$$x_f = \sqrt{3/2}\underline{X} = \sqrt{3/2}Xe^{j\varphi_X}. \tag{25}$$

Finally, the relation between the *forward* component of the transformed *Ku* variable and their *Park* components is [53]

$$x_d = \sqrt{2}Re\{x_f\};\ x_q = \sqrt{2}Im\{x_f\} \rightarrow x_f = \frac{1}{\sqrt{2}}\left(x_d + jx_q\right) \tag{26}$$

where the subscripts d and q stand for the *direct* and *quadrature* components, respectively, of the transformed *Park* variable.

REFERENCES

[1] "Renewable energy policy network for the 21st century (REN21)," Renewables 2021, Paris, France, Global Status Rep., Jun. 2021. Accessed: Aug. 16, 2021. [Online]. Available: http://www.ren21.net/ AQ2

[2] "Market report series: Renewables 2020. Analysis and forecasts to 2025," Int. Energy Agency (IEA), Paris, France, Rep., Nov. 2020. Accessed: Aug. 16, 2021. [Online]. Available: https://www.iea.org/

[3] "Global energy transformation. A roadmap to 2050," Int. Renew. Energy Agency (IRENA), Abu Dhabi, UAE, Rep., Apr. 2019. Accessed: Aug. 16, 2021. [Online]. Available: http://www.irena.org/

[4] F. Blaabjerg, Y. Yang, D. Yang, and X. Wang, "Distributed power-generation systems and protection," *Proc. IEEE*, vol. 105, no. 7, pp. 1311–1331, Jul. 2017.

[5] M. H. J. Bollen, and F. Hassan, *Integration of Distributed Generation in the Power System*. Hoboken, NJ, USA: Wiley, 2011, pp. 437–447.

[6] R. Teodorescu, M. Liserre, and P. Rodríguez, *Grid Converters for Photovoltaic and Wind Power Systems*. Chichester, U.K.: Wiley, 2011, pp. 237–287.

[7] *The Grid Code. Issue 5, Rev. 20. Great Britain*, Nat. Grid Electricity Syst. Oper., Warwick, U.K., Feb. 2017. Accessed: Aug. 16, 2021. [Online]. Available: https://www.nationalgrideso.com

[8] *Technical Regulation 3.2.5 for Wind Power Plants Above 11 kW*, Energinet, Fredericia, Denmark, Jul. 2016. Accessed: Aug. 16, 2021. [Online]. Available: https://en.energinet.dk/

[9] *Technical Regulation 3.2.2 for PV Power Plants Above 11 kW*, Energinet, Fredericia, Denmark, Jul. 2016. Accessed: Aug. 16, 2021. [Online]. Available: https://en.energinet.dk/

[10] TenneT. (Dec. 2012). *Requirements for Offshore Grid Connections in the Grid of TenneT TSO GmbH*. Accessed: Aug. 16, 2021. [Online]. Available: https://www.tennet.eu/

[11] *Technical Requirements for Wind Power and Photovoltaic Installations and Any Generating Facilities Whose Technology Does Not Consist on a Synchronous Generator Directly Connected to the Grid, Offprint Form the O.P. 12.2 Outline*, Red Eléctrica, Alcobendas, Spain, Oct. 2008. Accessed: Aug. 16, 2021. [Online]. Available: https://www.ree.es/ AQ3

[12] L. L. Grigsby, *Electric Power Generation, Transmission, and Distribution*, 3rd ed. Boca Raton, FL, USA: CRC Press, 2012, p. 11.

[13] M. Tsili and S. Papathanassiou, "A review of grid code technical requirements for wind farms," *IET Renew. Power Gener.*, vol. 3, no. 3, pp. 308–332, Sep. 2009.

[14] M. Altin, Ö. Göksu, R. Teodorescu, P. Rodríguez, B.-B. Jensen, and L. Helle, "Overview of recent grid codes for wind power integration," in *Proc. 12th Int. Conf. Optim. Elect. Electron. Equip.*, vol. 1. Brasov, Romania, May 2010, pp. 1152–1160.

[15] A. Etxegarai, E. Torres, I. Zamora, J. I. S. Martín, and P. Eguia, "Review of procedures for verification of grid code compliance of renewable generation," in *Proc. Int. Conf. Renew. Energies Power Qual.*, vol. 1. Córdoba, Spain, Apr. 2014, pp. 855–861.

[16] S. I. Nanou and S. A. Papathanassiou, "Grid code compatibility of VSC-HVDC connected offshore wind turbines employing power synchronization control," *IEEE Trans. Power Syst.*, vol. 31, no. 6, pp. 5042–5050, Nov. 2016.

[17] J. Kabouris and F. D. Kanellos, "Impacts of large-scale wind penetration on designing and operation of electric power systems," *IEEE Trans. Sustain Energy*, vol. 1, no. 2, pp. 107–114, Jul. 2010.

[18] S. M. Muyeen, R. Takahashi, T. Murata, and J. Tamura, “A variable speed wind turbine control strategy to meet wind farm grid code requirements,” *IEEE Trans. Power Syst.*, vol. 25, no. 1, pp. 331–340, Feb. 2010.

[19] M. Bakkar, S. Bogarra, A. Rolán, F. Córcoles, and J. Saura, “Voltage sag influence on controlled three-phase grid-connected inverters according to the Spanish grid code,” *IET Gener. Transm. Distrib.*, vol. 14, no. 10, pp. 1882–1892, May 2020.

[20] M. Bakkar, S. Bogarra, F. Córcoles, J. Saura, and M. Moreno, “Power control strategies during voltage sags according to Spanish grid code,” in *Proc. Int. Conf. Renew. Energies Power Qual.*, Salamanca, Spain, Mar. 2018, pp. 493–498.

[21] Y. Bae, T.-K. Vu, and R.-Y. Kim, “Implemental control strategy for grid stabilization of grid-connected PV system based on German grid code in symmetrical low-to-medium voltage network,” *IEEE Trans. Energy Convers.*, vol. 28, no. 3, pp. 619–631, Sep. 2013.

[22] A. Rolán, J. Pedra, and F. Córcoles, “Detailed study of DFIG-based wind turbines to overcome the most severe grid faults,” *Int. J. Elect. Power Energy Syst.*, vol. 62, no. 1, pp. 868–878, Nov. 2014.

[23] A. Rolán, F. Córcoles, and J. Pedra, “Behaviour of the doubly fed induction generator exposed to unsymmetrical voltage sags,” *IET Elect. Power Appl.*, vol. 6, no. 8, pp. 561–574, Sep. 2012.

[24] A. Rolán, F. Córcoles, and J. Pedra, “Doubly fed induction generator subject to symmetrical voltage sags,” *IEEE Trans. Energy Convers.*, vol. 26, no. 4, pp. 1219–1229, Dec. 2011.

[25] A. Camacho, M. Gastilla, J. Miret, A. Borrell, and. L. G. de Vicuña, “Active and reactive power strategies with peak current limitation for distributed generation inverters during unbalanced grid faults,” *IEEE Trans. Ind. Electron.*, vol. 62, no. 3, pp. 1515–1525, Mar. 2015.

[26] F. K. A. Lima, A. Luna, P. Rodríguez, E. H. Watanabe, and F. Blaabjerg, “Rotor voltage dynamics in the doubly fed induction generator during grid faults,” *IEEE Trans. Power Electron.*, vol. 25, no. 1, pp. 118–130, Jan. 2010.

[27] J. Hu and Y. He, “DFIG wind generation systems operating with limited converter rating considered under unbalanced network conditions—Analysis and control design,” *Renew. Energy*, vol. 36, no. 2, pp. 829–847, Feb. 2011.

[28] S. Chondrogiannis and M. Barnes, “Specification of rotor side voltage source inverter of a doubly-fed induction generator for achieving ride-through capability,” *IET Renew. Power Gener.*, vol. 2, no. 3, pp. 139–150, Sep. 2008.

[29] A. Rolán, P. Giménez, S. J. Yagüe, S. Bogarra, J. Saura, and M. Bakkar, “Voltage recovery influence on three-phase grid-connected inverters under voltage sags,” *IET Gener. Transm. Distrib.*, vol. 13, no. 3, pp. 435–443, Feb. 2019.

[30] A. Rolán, P. Giménez, S. J. Yagüe, and S. Bogarra, “Modeling and control of a three-phase grid-connected inverter under fault conditions,” in *Proc. Int. Symp. Power Electron. Elect. Drives Autom. Motion*, Amalfi, Italy, Jun. 2018, pp. 479–484.

[31] M. Mohseni, S. M. Islam, and M. A. S. Masoum, “Impacts of symmetrical and asymmetrical voltage sags on DFIG-based wind turbines considering phase-angle jump, voltage recovery, and sag parameters,” *IEEE Trans. Power Electron.*, vol. 26, no. 5, pp. 1587–1598, May 2011.

[32] *IEEE Recommended Practice for Monitoring Electric Power Quality*, IEEE Standard 1159–2019, 2019.

[33] L. Guasch, F. Córcoles, J. Pedra, and L. Sáinz, “Effects of symmetrical voltage sags on three-phase three-legged transformers,” *IEEE Trans. Power Del.*, vol. 19, no. 2, pp. 875–883, Apr. 2004.

[34] L. Guasch, F. Córcoles, and J. Pedra, “Effects of symmetrical and unsymmetrical voltage sags on induction machines,” *IEEE Trans. Power Del.*, vol. 19, no. 2, pp. 774–782, Apr. 2004.

[35] J. Pedra, F. Córcoles, and F. J. Suelves, “Effects of balanced and unbalanced voltage sags on VSI-fed adjustable-speed drives,” *IEEE Trans. Power Del.*, vol. 20, no. 1, pp. 224–233, Jan. 2005.

[36] M. H. J. Bollen, *Understanding Power Quality Problems: Voltage Sags and Interrumptions*. New York, NY, USA: Wiley, 2000, pp. 139–251.

[37] M. H. J. Bollen, “Voltage recovery after unbalanced and balanced voltage dips in three-phase systems,” *IEEE Trans. Power Del.*, vol. 18, no. 4, pp. 1376–1381, Oct. 2003.

[38] B. Subudhi and R. Pradhan, “A comparative study on maximum power point tracking techniques for photovoltaic power systems,” *IEEE Trans. Sustain. Energy*, vol. 4, no. 1, pp. 89–98, Jan. 2013.

[39] *American Society for Testing and Materials (ASTM). Reference Air Mass 1.5 Spectra*. Accessed: Aug. 16, 2021. [Online]. Available: https://www.nrel.gov/

[40] M. G. Villalba, J. R. Gazoli, and E. R. Filho, “Comprehensive approach to modeling and simulation of photovoltaic arrays,” *IEEE Trans. Power Electron.*, vol. 24, no. 5, pp. 1198–1208, May 2009.

[41] H. Akagi, Y. Kanazawa, and A. Nabae, “Instantaneous reactive power compensators comprising switching devices without energy storage components,” *IEEE Trans. Ind. Appl.*, vol. IA-20, no. 3, pp. 625–630, May 1984.

[42] H. Akagi, E. H. Watanabe, and M. Aredes, *Instantaneous Power Theory and Applications to Power Conditioning*. 2nd ed. Hoboken, NJ, USA: Wiley, 2017, pp. 37–109.

[43] S.-K. Chung, “A phase tracking system for three phase utility interface inverters,” *IEEE Trans. Power Electron.*, vol. 15, no. 3, pp. 431–438, May 2000.

[44] H.-S. Song and K. Nam, “Dual current control scheme for PWM converter under unbalanced input voltage conditions,” *IEEE Trans. Ind. Electron.*, vol. 46, no. 5, pp. 953–959, Oct. 1999.

[45] E. Koutroulis and K. Kalaitzakis, “Design of a maximum power tracking system for wind-energy-conversion applications,” *IEEE Trans. Ind. Electron.*, vol. 53, no. 2, pp. 486–494, Apr. 2006.

[46] E. Muljadi and C. P. Butterfield, “Pitch-controlled variable-speed wind turbine generation,” *IEEE Trans. Ind. Appl.*, vol. 37, no. 1, pp. 240–246, Jan./Feb. 2001.

[47] R. Peña, J. C. Clare, and G. M. Asher, “Doubly fed induction generator using back-to-back PWM converters and its application to variable-speed wind-energy generation,” *IEE Proc. Elect. Power Appl.*, vol. 143, no. 3, pp. 231–241, May 1996.

[48] T. I. Reigstad, “Fault current contribution from DG,” SINTEF Energi, Trondheim, Norway, Rep., May 2016. Accessed: Aug. 16, 2021. [Online]. Available: https://www.ntnu.edu/

[49] M. H. J. Bollen *et al.* (Apr. 2010). *Voltage Dip Immunity of Equipment in Installations, CIGRE/CIRED/UIE Joint Working Group C4.110, Tech. Broch. 412*. Accessed: Aug. 16, 2021. [Online]. Available: https://e-cigre.org/

[50] A. Petersson, T. Thiringer, L. Harnerfors, and T. Petru, “Modeling and experimental verification of grid interaction of a DFIG wind turbine,” *IEEE Trans. Energy Convers.*, vol. 20, no. 4, pp. 878–886, Dec. 2005.

[51] B. Wu, Y. Lang, N. Zargari, and S. Kouro, *Power Conversion and Control of Wind Energy Systems*. Hoboken, NJ, USA: Wiley, 2011, p. 324.

[52] J. G. Slootweg, H. Polinder, and W. L. Kling, “Representing wind turbine electrical generating systems in fundamental frequency simulations,” *IEEE Trans. Energy Convers.*, vol. 18, no. 4, pp. 516–524, Dec. 2003.

[53] Y. H. Ku, “Transient analysis of rotating machines and stationary networks by means of rotating reference frames,” *Trans. Amer. Inst. Elect. Eng.*, vol. 70, no. 1, pp. 943–957, Jul. 1951.